# Mem-MLP: Real-Time 3D Human Motion Generation from Sparse Inputs

Sinan Mutlu<sup>1\*</sup> Georgios F. Angelis<sup>2\*</sup> Savas Ozkan<sup>1†</sup> Paul Wisbey<sup>1</sup>
Anastasios Drosou<sup>2</sup> Mete Ozay<sup>1</sup>

<sup>1</sup> Samsung R&D Institute UK (SRUK)

<sup>2</sup> Information Technologies Institute, CERTH
s.mutlu@samsung.com, angelisg@iti.gr, savas.ozkan@samsung.com

### **Abstract**

Realistic and smooth full-body tracking is crucial for immersive AR/VR applications. Existing systems primarily track head and hands via Head Mounted Devices (HMDs) and controllers, making the 3D full-body reconstruction incomplete. One potential approach is to generate the fullbody motions from sparse inputs collected from limited sensors using a Neural Network (NN) model. In this paper, we propose a novel method based on a multi-layer perceptron (MLP) backbone that is enhanced with residual connections and a novel NN-component called Memory-Block. In particular, Memory-Block represents missing sensor data with trainable code-vectors, which are combined with the sparse signals from previous time instances to improve the temporal consistency. Furthermore, we formulate our solution as a multi-task learning problem, allowing our MLP-backbone to learn robust representations that boost accuracy. Our experiments show that our method outperforms state-of-theart baselines by substantially reducing prediction errors. Moreover, it achieves 72 FPS on mobile HMDs that ultimately improves the accuracy-running time tradeoff.

# 1. Introduction

The applications of real-time tracking of 3D human motions are vast and diverse, with significant implications for various fields, including biomechanics, video games, and sports analysis [30]. In the context of Virtual Reality (VR) and Augmented Reality (AR) systems, the ability to track 3D human motions in real-time is essential for creating an immersive and interactive experience. By mirroring the user's physical movements in the virtual environment, VR/AR systems can foster a sense of presence and engagement, enabling users to intuitively interact with virtual objects and environments.

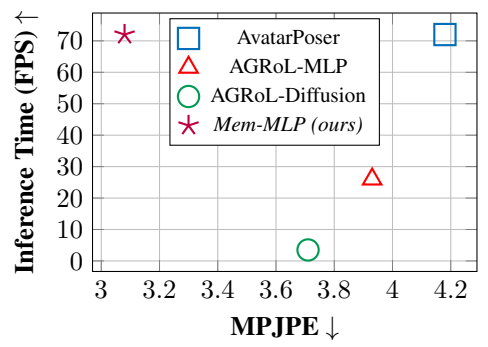


Figure 1. On-device comparison of state-of-the-art methods for full-body motion generation. For each method, we report the performance by plotting inference time (FPS) against mean per-joint position error (MPJPE). All the timings are obtained by running the inference on the Quest-3 headset. Note that a lower MPJPE value indicates better accuracy, whereas a higher FPS value indicates better efficiency.

Delivering a fully immersive experience in Virtual Reality (VR) and Augmented Reality (AR) applications relies heavily on tracking full-body movements. However, conventional AR/VR setups are limited by the number of tracking devices, typically consisting of a Head Mounted Display (HMD) and hand controllers equipped with Inertial Measurement Unit (IMUs) devices. As a result, only the movements of head and hands can be tracked and mirrored into the virtual environment, leaving other body parts unobserved. This significant gap in capturing full-body motion hinders the creation of a truly immersive experience, as the virtual environment cannot accurately reflect the user's movements. One potential solution is to attach additional tracking sensors to other body parts, such as the pelvis, legs, or arms [19, 41, 44]. However, this approach is often impractical and requires customized setups for different VR/AR scenarios, highlighting the need for a more flexible and efficient solution. To overcome this limitation, a promising approach is to generate 3D motions of the entire human body from the limited data collected by the available tracking sensors. Nevertheless, this task is challenging due to the vast number of possible 3D human motions that

<sup>\*</sup>Equal Contributions for Main Authorships

<sup>†</sup>Senior Authorship

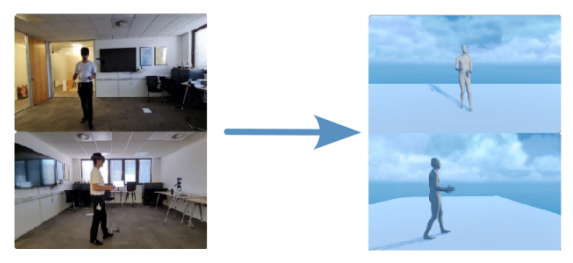


Figure 2. Given the sparse inputs of body joint representations, our model can accurately generate diverse motions in real-time on a head mounted device.

can be generated from the sparse input data. Therefore, a robust generation model is necessary to effectively handle these complex scenarios and produces accurate and realistic full-body motions.

In this work, we present a novel method which is designed for generating 3D full-body motions from sparse inputs in real-time as illustrated in Fig. 2. Our method builds upon a recently proposed model for 3D human-body motion generation, AGRoL [13], which employs a multi-layer perceptron (MLP)-based architecture with residual connections. To improve the accuracy of generated motion sequences, we propose a novel NN-component named Memory Block that enhances temporal consistency and reduces errors across various metrics, resulting in more realistic and coherent motion generation. Precisely, the Memory Block component employs code-vectors that represent the missing sensor inputs and combines them with the sparse signals from previous time instances. This information is then leveraged in the hidden layers of the neural network (NN)based backbone. Experimental results on the benchmark AMASS dataset [27] demonstrate that the *Memory Block* yields significant performance gains. Moreover, due to its computationally efficient structure, this lightweight component is particularly well-suited for real-time applications.

In contrast to the most state-of-the-art work [8, 19, 20], AGRoL [13] has shown that adding 3D geometric losses to angle-based losses during training yields only marginal or no performance improvements. One possible explanation is that geometric loss functions (such as distance-based losses for joint positions) and angle-based losses may conflict during the optimization step. Specifically, minimizing joint location errors can lead to suboptimal joint angles, particularly if the model struggles to balance these objectives. To address this issue, we employ a loss weighting mechanism using homoscedastic uncertainty for multi-task learning, which enables our method to leverage both angle-based and distance-based losses. This allows our model to learn more generic and robust representations, ultimately improving the performance of full-body motion generation.

Lastly, we need to emphasize that our model is considerably lightweight compared to state-of-the-art complex methods that are based on transformers or diffusion mod-

els. Our model not only reduces computational overhead but also makes our method highly suitable for real-time applications with high accuracy. We summarize our contributions as follows:

- We propose a novel NN-based component that represents missing sensor inputs with trainable code-vectors and later utilizes them to add temporal information from previous time instances. It ultimately provides temporal consistency and improves the performance from 22.70 to 7.00 for the Jitter metric. The details of our memory-block are presented in Sec. 3.2.1.
- A multi-head predictor is introduced for multi-task learning, leveraging the same backbone network to generate both rotation and position predictions. This approach learns more comprehensive representations and delivers an additional improvement from 7.00 to 6.03 in the Jitter metric.
- Our method can be seamlessly integrated into mobile devices, achieving the minimum required runtime efficiency [4] (i.e., 72 FPS) for interactive applications on head-mounted devices. Additionally, in comparison to the state-of-the-art AvatarPoser [19], which also meets the requirements, our method improves the metric accuracy by reducing the position error by 26%, as shown in Fig. 1. To this end, the trade-off between accuracy and running time is optimized.

### 2. Related Work

### 2.1. Motion Generation with Sparse Inputs

Motion reconstruction from sparse signal inputs has gained significant attention with the development of the HMDs. Some of the recent research work focused on using six IMU devices, attached to the wrists, lower legs, back and head [41]. Similarly [44] used only four sensors, pelvis, head and hands. In practical extended reality (XR) scenarios, typically only three tracking signals are available: the head and two wrists. Simulation driven pipelines such as [24, 42] leverage physics-based simulation and reinforcement learning to reconstruct plausible motions under sparse inputs. Learning based models such as AvatarPoser [19] address the 3-point setting with transformer architectures, while other approaches cast sparse tracking as a synthesis problem-for example, flow-based models [7] and VAEbased methods [11]. Overall, many state-of-the-art methods [10, 11, 19, 21, 43, 46] rely on transformer-style designs that are comparatively slower on mobile hardware. In contrast, our model uses an MLP backbone with skip connections (as in [13]) delivering competitive accuracy with substantially lower computational cost.

More recent works such as [12, 13, 15, 23, 37] employ diffusion-based architectures. [15] generates separate VQ-VAE [40] codebooks for the lower and upper body parts

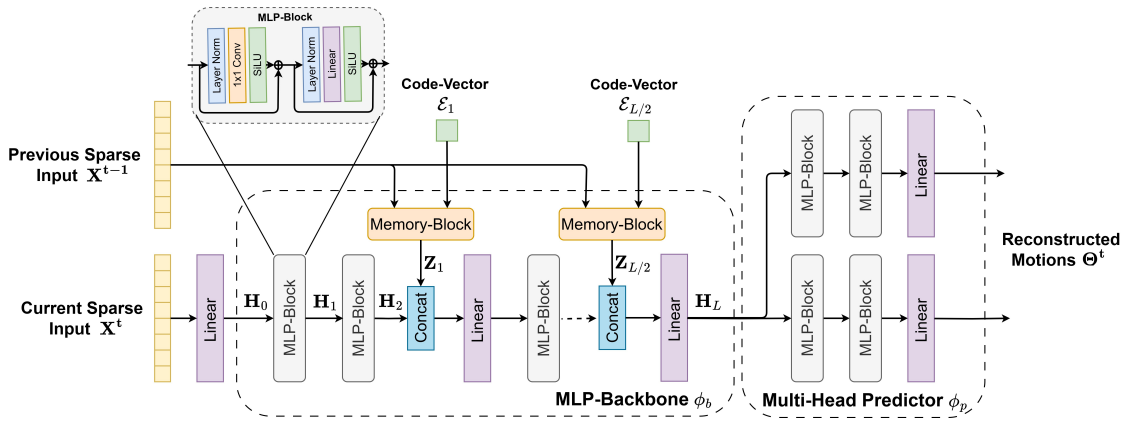


Figure 3. The architecture of our method. The details of our method is explained in Sec. 3.

with diffusion process: first diffusion model generates VO-VAE code-books using the sparse sensor data, second one generates the VQ-VAE code-books for the lower body using the sparse and upper body code books that are created in the first step. Then these two code-books are given to a decoder to generate all joint angles. Our approach, motivated by [15], employs code-books as well, hereafter referred to as code-vectors, to integrate human pose and motion priors into the model. This approach allows the generation of smooth and plausible motion sequences using a lightweight autoencoder built from multilayer perceptrons. [12] is based on a U-net shaped architecture which utilizes the Motion Mamba Blocks. Although all of these methods show promising results, they are not feasible for running on mobile devices due to the computational requirement for the diffusion process. In contrast to these methods, our method aligns more closely with [10, 11, 19, 46], generating a motion sequence in a single step. Our design choice not only simplifies the architecture but also enhances the computational efficiency, making it more suitable for real-time applications on mobile devices.

In a similar domain to 3D human motion generation from sparse inputs, the computer vision and graphics community has focused on generating 3D human motions conditioned on various inputs. These include text [32, 34, 45], action categories [17], incomplete pose sequence completion [14, 31] and other control signals [13, 19, 36]. Among these approaches, text-to-motion has emerged as the leading focus in recent years [33, 34, 45], with the aim of learning a shared latent representation between language and motion.

In summary, state-of-the-art works in our domain, as discussed in this section, require either more than three joint inputs to achieve comparable accuracy on the metrics or rely on computationally intensive models, such as transformers. Some of these models also incorporate diffusion samplers, which significantly impact run-time performance on XR devices. In contrast, our proposed method utilizes only three sensor inputs and is built on a simple architecture composed of MLP blocks, complemented by additional

lightweight components. Moreover, the simplicity of our method improves its adaptability and feasibility for various XR applications.

#### 2.2. Motion Dataset

Modeling human motion has been a persistent challenge in the fields of computer vision and computer graphics. The rise of deep learning has highlighted the growing importance of data for training neural networks to recognize, interpret, and produce human movements. Most commonly existing datasets contain the videos of the human subjects, which are recorded in lab environment, with the 2D or 3D joint key-points [18], and each of them employ different body parametrization. For this reason to train our models we used AMASS [27] dataset which consolidates 15 distinct optical marker-based MOCAP datasets into a single framework with a common parametrization: a skinned vertex based model that accurately represents a wide variety of body shapes in natural human poses, SMPL[26].

## 3. Method

### 3.1. Problem Formulation

The function of full-body motion generation f aims to reconstruct complete full-body motions  $\mathbf{\Theta^t}$  from sparse tracking input signals  $\mathbf{X^t}$ , which can be represented by  $\mathbf{\Theta^t} = f(\mathbf{X^t})$ . This function f typically operates in a time window  $\mathbf{t}$  of length T, covering time instances from t-T to t to achieve stable motion generation and ensure temporal smoothness. If we define the column-wise concatenation operator by  $\mathbf{X} = [X_i]_{i=1}^N \triangleq [X_1,...,X_N]$ , within a time window  $\mathbf{t}$ , the function utilizes the entire set of observed input signals  $\mathbf{X^t} = [X^i]_{i=t-T}^t \in \mathbb{R}^{T \times S}$  to reconstruct the corresponding full-body motions  $\mathbf{\Theta^t} = [\mathbf{\Theta^i}]_{i=t-T}^t \in \mathbb{R}^{T \times F}$  for time instances. Here, the dimensions of the input signals and reconstructed motions are denoted by S and F, respectively.

**Input Signals**: At each time instance t, the input signal  $X^t$  consists of three sparse signals, collected from

the head, left and right hand sensors, and represented by  $X^t = [\mathbf{x}_h^t, \mathbf{x}_l^t, \mathbf{x}_r^t]$ . Each joint signal  $\mathbf{x}_j^t$  (where  $j \in \{h, l, r\}$ ) at a time instance t is represented by an axis-angle representation  $\psi_j^t \in \mathbb{R}^3$  and a Cartesian coordinate  $\mathbf{p}_j^t \in \mathbb{R}^3$  defined within the global coordinate system. Following previous work [47], the axis-angle representation  $\psi_j^t$  is converted to a 6D representation  $\theta_j^t \in \mathbb{R}^6$  by discarding the last row of a rotation matrix. Furthermore, the linear velocity  $\mathbf{v}_j^t \in \mathbb{R}^3$  and angular velocity  $\mathbf{w}_j^t \in \mathbb{R}^6$  representations are calculated to enforce temporal smoothness, as proposed in [19]. Consequently, each sensor signal at a time instance t is represented by  $\mathbf{x}_j^t = [\mathbf{p}_j^t, \theta_j^t, \mathbf{v}_j^t, \mathbf{w}_j^t]$ . The dimension of the input signal S is 54.

**Reconstructed Motion**: Full-body motions at a time instance t are represented by a tuple  $\Theta^t = (\theta_i^t, \mathbf{p}_i^t)_{i=1}^{22} \in \mathbb{R}^{22 \times 9}$ , which comprises the 3D Cartesian coordinates  $\mathbf{p}_i^t$  and 6D rotation parameters  $\theta_i^t$  for each of the 22 joints of the upper body  $(J_{\rm up})$  and lower body  $(J_{\rm lo})$ . To this end, the dimension of the reconstructed full-body motion F is equal to 198.

#### 3.2. Our Method

In our method, the full-body motion generation function f is implemented by an MLP-based network model  $\phi$  parameterized by  $\varphi_{\phi}$ . Our architecture is illustrated in Figure 3. This model is inspired by the architecture proposed in [13], in order to have an efficient and effective full-body motion generation that makes our solution suitable for real-time applications. Our model can be decomposed into two submodels for simplicity: MLP-backbone  $\phi_b$  and multi-task predictor  $\phi_p$ . To this end, it can be represented by  $\phi = \phi_p \circ \phi_b$ .

# 3.2.1. MLP-backbone:

Our MLP-backbone model  $\phi_b$  consists of stacked MLP-blocks and memory-blocks. Details of memory-block will be explained as a separate section. Each MLP-block contains 1D convolution layer, Layer Normalization, SiLU activation, and Linear layer. Intuitively, 1D convolutional layers capture temporal patterns, while linear layers process spatial information from input signals.

In our implementation, a separate linear layer is initially applied to the sparse signal  $\mathbf{X}^t$  to project it onto a latent representation  $\mathbf{H}_0 \in \mathbb{R}^{T \times d}$ , where d denotes the dimensionality of the latent space. This latent representation  $\mathbf{H}_0$  is then iteratively refined through L numbers of layers of MLP-blocks. The final output of the MLP-backbone is represented by  $\mathbf{H}_L \in \mathbb{R}^{T \times d}$ , which captures the processed latent information.

**Memory-Block:** Generating full-body motions from sparse signals requires the effective use of temporal information to reduce the solution space. However, relying solely on temporal context from sparse signals may be insufficient in edge cases. Increasing the length of the temporal window

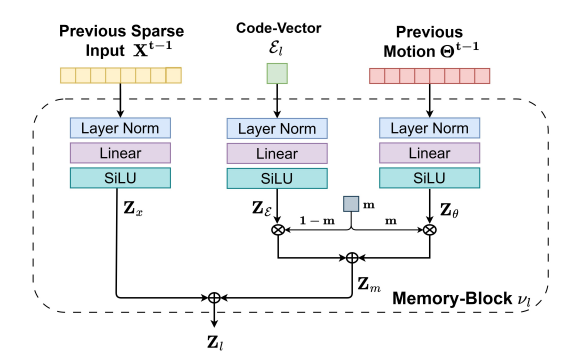


Figure 4. The architecture of our memory-block component for the  $l^{\rm th}$  layer during training where l=1,..,L/2. Its details are explained in Sec. 3.2.1.

T can lead to overfitting to past inputs, resulting in overly smoothed reconstructions. To mitigate this, we introduce a neural component called the *Memory-Block*, illustrated in Fig. 4. It augments sparse observations with learned priors to recover full-body joint dynamics.

In this component, missing signals from joints other than the head and hands are approximated using trainable code-vectors derived from a frozen VQ-VAE model [15]. Unlike prior use cases our main motivation for exploiting VQ-VAE module is not to generate realistic motions but to encode plausible motion priors conditioned on both sparse signals and corresponding full-body motions at time t. Specifically, given sparse features  $\mathbf{X}^{t-1}$  and full-body motions  $\mathbf{\Theta}^{t-1}$ , the encoder produces a latent vector  $\mathbf{z}_s =$  $f_{\text{enc}}([\mathbf{X}^{t-1}; \mathbf{\Theta}^{t-1}]), z_s \in \mathbb{R}^{d_{z_s}}, \text{ where } d_{z_s} = 256. \text{ This}$ is quantized via a learned codebook  $\mathcal{C} = \{\mathbf{e}_1, \dots, \mathbf{e}_K\} \subset$  $\mathbb{R}^{d_{z_s}}$ , where K=64 by selecting the closest codebook entry:  $\mathcal{E}_l = \mathbf{e}_k \in \mathbb{R}^{256}$  where  $k = \arg\min_j \|\mathbf{z}_s - \mathbf{e}_j\|_2$ . Each code-vector  $\mathcal{E}_l$  thus represents a discrete prior embedding for the  $l^{th}$  memory-block. For more details on the design of VQ-VAE module please refer to the Architectural Design section in the supplementary material.

During training, the memory-block  $\nu_l$  at layer l receives sparse features  $\mathbf{X}^{t-1}$ , ground-truth motions  $\Theta^{t-1}$ , and the corresponding code-vector  $\mathcal{E}_l$  to produce a memory-feature:  $\mathbf{Z}_l = \nu_l(\mathbf{X}^{t-1}, \boldsymbol{\Theta}^{t-1}, \mathcal{E}_l)$ . Each input is projected to a latent representation using a dedicated MLP (linear layer, layer norm, and SiLU). Let  $\mathbf{Z}_x, \mathbf{Z}_\theta$ , and  $\mathbf{Z}_\mathcal{E}$  be the resulting latent features. To simulate inference conditions, we blend these features using a random coefficient  $\mathbf{m} \in \mathbb{R}^{T \times k}$  is sampled from a uniform distribution on the interval [0,1] to compute  $\mathbf{Z}_m = \mathbf{m} * \mathbf{Z}_\theta + (1-\mathbf{m}) * \mathbf{Z}_\mathcal{E}$ , where \* denotes element-wise multiplication. The final memory feature is then given by  $\mathbf{Z}_l = \mathbf{Z}_x + \mathbf{Z}_m$ .

At inference time, since ground-truth motions  $\Theta^{t-1}$  are unavailable, we use the predicted full-body motion  $\widehat{\Theta}^{t-1}$  from the previous step. If no previous prediction exists (e.g., at the initial frame), we use a zero tensor as fallback. Thus, the memory-block becomes autoregressive and oper-

ates as  $\mathbf{Z}_l = \nu_l(\mathbf{X}^{t-1}, \widehat{\boldsymbol{\Theta}}^{t-1}, \mathcal{E}_l)$ , with latent merging and memory-feature computed as before. This autoregressive structure enables the model to leverage temporal continuity while compensating for missing sensor data using learned priors. The resulting memory feature  $\mathbf{Z}_l$  is concatenated into the MLP backbone, enhancing intermediate representations across layers.

This design forms an **autoregressive memory mechanism**, where each memory block utilizes past predictions to generate informative context features for the current frame. The resulting memory-feature  $\mathbf{Z}_l$  is concatenated with the hidden representation at the corresponding MLP layer and passed forward through the network. To this end, our novel architecture exploits both information from current and previous time windows and combines them in the latent space. In particular, missing information from joint locations is filled with trainable code-vectors during inference.

#### 3.2.2. Multi-Task Predictor

Existing literature predominantly addresses full-body motion generation as a single-task learning problem, focusing on estimating the 6D rotations  $\theta_i^t, \forall i$  at a time instance t [11–13, 15, 19, 46]. In contrast, we adopt a multi-task learning approach, where we not only estimate the rotations but also generate the corresponding global positions  $\mathbf{p}_{i}^{t}, \forall i$  at a time instance t. Our method exploits shared representations to improve the generalization, enabling the model to learn complementary tasks simultaneously and enhancing the overall performance. Ultimately, the prediction of global positions helps to refine the rotational representations by providing spatial context information. On the other hand, accurate rotations lead to more precise positioning, creating a benefit for both tasks. Throughout this process, the MLP-backbone  $\phi_b$  is enabled to learn richer features essential for both predictions, since it is responsible for capturing contextual information across the entire input sequence.

For this purpose, our multi-task predictor  $\phi_p$  has two MLP-based branches: one branch generates the joint angle rotations, while the other one generates the joint positions. Each branch has two MLP-blocks and one linear layer. Ultimately, this ensures that the shared representations utilized in both branches improves the precision and robustness of the predictions.

### 3.3. Loss Design

We utilize multiple loss functions based on angle and position to train the parameters of our network model  $\varphi_{\phi}$ . First, an angle loss  $\mathcal{L}_{\theta}$  is utilized to minimize the prediction error between ground-truth rotations  $\theta_i^t$  and predicted rotations  $\hat{\theta}_i^t$  for full-body joint locations by

$$\mathcal{L}_{\theta} = \frac{1}{T} \sum_{t=1}^{T} \sum_{i=1}^{22} \|\theta_i^t - \hat{\theta}_i^t\|_1, \tag{1}$$

where T indicates the total number of time instances in the training sequence. Furthermore, we introduce a rotational velocity loss  $\mathcal{L}_{rv}$  to ensure smooth transitions in temporal motions. It provides an alignment between the predicted angular velocity and the ground truth. This loss is defined as follows:

as follows: 
$$\mathcal{L}_{rv} = \frac{1}{T-1} \sum_{t=1}^{T-1} \sum_{i=1}^{22} \| (\theta_i^{t+1} - \theta_i^t) - (\hat{\theta}_i^{t+1} - \hat{\theta}_i^t) \|_1.$$
 (2)

For the second branch of our model that computes positions, we include two additional losses to optimize the model parameters. Specifically, a position loss  $\mathcal{L}_p$  minimizes the distance between the predicted global positions  $\hat{\mathbf{p}}_i^t$  and the ground truth positions  $\mathbf{p}_i^t$ , formulated by:

$$\mathcal{L}_p = \frac{1}{T} \sum_{t=1}^{T} \sum_{i=1}^{22} \|\mathbf{p}_i^t - \hat{\mathbf{p}}_i^t\|_1.$$
 (3)

To further enhance the smoothness of motion, we introduce a velocity loss  $\mathcal{L}_{fv}$ , which encourages the predicted positional velocity to closely match the ground truth velocity. By doing so, we improve the smoothness of the generated motions. The loss is defined by:

$$\mathcal{L}_{fv} = \frac{1}{T-1} \sum_{t=1}^{T-1} \sum_{i \in J_{lo}} \| (\mathbf{p}_i^{t+1} - \mathbf{p}_i^t) - (\hat{\mathbf{p}}_i^{t+1} - \hat{\mathbf{p}}_i^t) \|_1$$

Here, the  $\mathcal{L}_{fv}$  loss uses only lower-body joint locations  $J_{\text{lo}}$ , as the uncertainty associated with reconstructing these joints is typically higher due to the absence of sparse input signals. The overall objective function  $\mathcal{L}$  used for training is defined by:  $\mathcal{L} = \lambda_{\theta} \mathcal{L}_{\theta} + \lambda_{rv} \mathcal{L}_{rv} + \lambda_{p} \mathcal{L}_{p} + \lambda_{fv} \mathcal{L}_{fv}$  (5)

where  $\lambda_{\theta}$ ,  $\lambda_{rv}$ ,  $\lambda_{p}$  and  $\lambda_{fv}$  are the coefficients that define the contribution of each loss term to the overall objective function. In particular, we utilize an automatic loss weighting mechanism by employing homoscedastic uncertainty [22] to adaptively set these coefficient during training.

# 4. Experiments

To compare our method with the existing studies, we utilize the AMASS dataset [27] as our benchmark for both training and evaluation. In particular, we use this benchmark to accommodate various scenarios.

**Scenario-1** (S1): Following the methodology proposed by [19], we utilize the CMU[2], BMLrub [38], and HDM05 [29] subsets by splitting the dataset into 90% for training and 10% for testing.

Scenario-2 (S2): Furthermore, we use the data split introduced in [13, 19]. In this setup, training is conducted using data from the CMU [2], MPI Limits [6], Total Capture [39],Eyes Japn [3], KIT [28], BioMotionLab [38], BML-Movi [16], EKUT [28], ACCAD [1], MPI Mosh [25], SFU [5], and HDM05 [29] subsets, while evaluation is performed

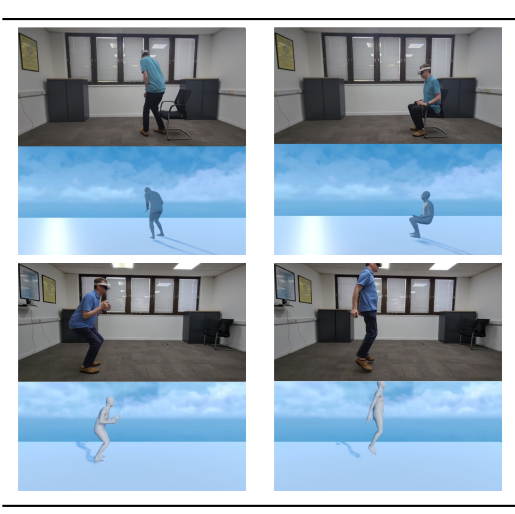


Figure 5. Visualization of our results on the Quest-3 headset and the hand controllers. Our model is capable to generate diverse motions such as walking, sitting and jumping in real-time.

on the HumanEVA [35] and Transition [27] subsets of the AMASS dataset [27]. This scenario enables us to evaluate the model scalability by testing its performance on motion clips recorded in an unfamiliar environment and also performed by unknown people. As noted in [15], training/testing partitions are imbalanced in this scenario, resulting a significant differences between test samples and those ones used in training. This can explain the performance drop for our model, similarly reported results in the state-of-the-art works [13, 15].

**Scenario-3** (S3): All sub-datasets in the AMASS dataset [27] are divided into training and test sets using the same ratios as in S1. For this specific scenario, we employ the data splits provided by [15].

### 4.1. Implementation Details

Following previous works, we set the time window length T to 41 to effectively capture the temporal information. This value is also used for the input dimensions of the memoryblocks. Our MLP-backbone consists of L=8 stacked MLP-blocks, where the outputs of the memory-blocks are concatenated with the outputs of the even-numbered MLP blocks. In multi-task predictor, each branch has two MLP-blocks followed by a linear layer. Our model is trained for  $300 \mathrm{K}$  steps using the AdamW optimizer, starting with an initial learning rate of 3e-4 that is reduced to 1e-5 after  $225 \mathrm{K}$  steps.

#### 4.2. Evaluation Metrics

For the evaluation of our method, we utilize the standard metrics used in the literature [13, 19]:

**Rotation-related metric:** The mean per joint rotation error [degrees] (*MPJRE*) measures the average relative rotation error for all joints.

Velocity-related metrics: These metrics consist of the

mean per joint velocity error [cm/s] (MPJVE) and Jitter. MPJVE calculates the average velocity error across all joint positions. Jitter serves as a measure of how smooth the motion is by computing the rate of change in acceleration over time for all body joints in global space,  $10^2 m/s^3$ .

**Position-related metrics**: The mean per joint position error [cm] captures the average deviation in position across all joint locations. *Root PE* specifically measures the positional error of the root joint, while *Hand PE* computes the average error for both hands. Additionally, *Upper PE* focuses on the joints in the upper body, and *Lower PE* targets those in the lower body.

#### 4.3. Evaluation Results

Evaluation Results on Scenario-1 (S1): Table 1 presents a detailed comparison of our Mem-MLP model with several baseline models for full-body motion generation. In particular, we evaluated two variants of our Mem-MLP model, each configured with different window lengths of T=41 and T=60. Furthermore, we include the results of our base model, AGRoL-MLP [13], which uses a time window of T=196, Fig-6.

The results demonstrate that both versions achieve comparable performance across most metrics; however, the Jitter metric reveals that longer input lengths yield smoother motion reconstruction. Furthermore, these two models achieve competitive results to the best performing ones in the standard metrics, surpassed only by the resource-intensive model BoDiffusion [9]. Although MDM [12] shows strong accuracy in the S1 dataset, its performance is not reported for other scenarios.

In Table 1, FLOPs are also reported for all models. *Mem-MLP-41* has the lowest FLOPs (0.25 G) compared to other models, demonstrating a clear advantage in terms of performance per computational cost. On the other hand, while *Mem-MLP-60* requires slightly higher computational cost (0.38 G), it achieves better accuracy in several metrics. To this end, while *Mem-MLP-41* offers a faster alternative, *Mem-MLP-60* provides superior accuracy, making it ideal for use cases that prioritize precision over speed. Note that the metric results for EgoPoser [21] are computed by running their model checkpoint on our S1 dataset, it was not reported in [21], for direct comparison and performance evaluation.

**Evaluation Results on Scenario-2 (S2):** Table 2 presents the experimental results for Scenario-2. Our method demonstrates competitive performance in S2, achieving superior results across all metrics compared to alternative models such as AvatarPoser [19] and AGRoL-MLP[13] that can have real-time inference. However, the observed degradation in accuracy can likely be attributed to the limited diversity within the overall data distribution of the S2 training dataset. Specifically, certain motion types such as crawling,

Method	MPJRE ↓	MPJPE ↓	MPJVE ↓	Hand PE $\downarrow$	Upper PE↓	Lower PE ↓	Root PE ↓	Jitter↓	#FLOPs (G) ↓
VAR-HMD [11]	4.11	6.83	37.99	_	_	_	_	-	_
AvatarPoser [19]	3.08	4.18	27.70	2.12	1.81	7.59	3.34	14.49	0.33
AGRoL-Diffusion [13]	2.66	3.71	18.59	1.31	1.55	6.84	3.36	7.26	1.00
AvatarJLM [46]	2.90	3.35	20.79	1.24	1.42	6.14	2.94	8.39	4.64
BoDiffusion [9]	2.70	3.63	14.39	1.32	1.53	7.07	-	4.90	0.46
SAGE Net [15]	2.53	3.28	20.62	1.18	1.39	6.01	2.95	6.55	4.10
EgoPoser [21]	3.09	5.24	24.93	4.97	3.79	7.80	3.78	15.37	0.33
MANIKIN-S [20]	_	3.36	23.18	0.02	1.32	6.72	_	7.95	0.33
MANIKIN-LN [20]	_	2.73	13.55	0.01	1.30	5.13	_	7.95	4.64
MMD [12]	2.30	3.17	17.32	0.79	1.25	5.94	2.86	6.52	7.98
HMD-Poser [10]	2.28	3.19	17.47	1.65	1.67	<u>5.40</u>	3.02	6.07	0.38
AGRoL-MLP-196 [13]	2.69	3.93	22.85	2.62	1.89	6.88	3.35	13.01	0.88
Mem-MLP-41 (ours)	2.57	3.08	15.02	0.27	1.25	5.72	2.85	6.03	0.25
Mem-MLP-60 (ours)	2.56	3.05	14.27	0.25	1.26	5.67	2.87	5.35	0.38

Table 1. Comparison with state-of-the-art methods for full-body motion estimation. Results on Scenario-1 (S1) are reported on AMASS dataset for Jitter [m/s³], MPJVE [cm/s], MPJPE [cm], Hand PE [cm], Upper PE [cm], Lower PE [cm], MPJRE [deg] and GFLOPs. The best results are in **bold**, and the second best results are underlined.

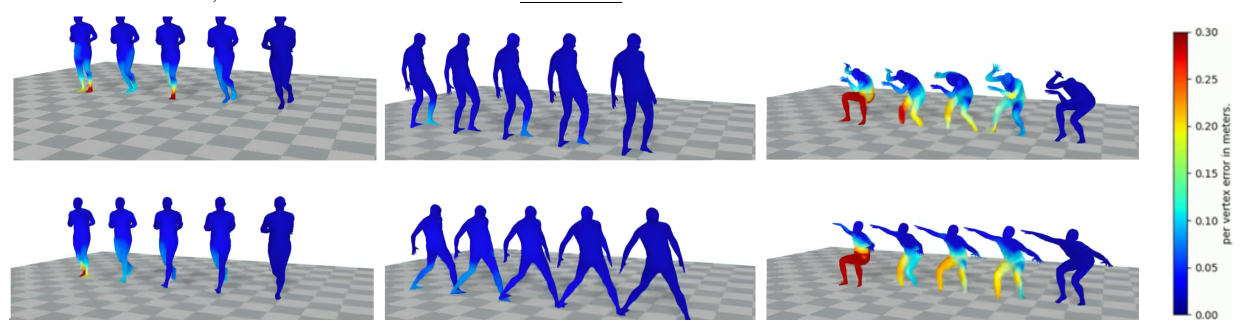


Figure 6. Motion reconstruction results of *running*, *sitestep* and *pterosaur* motions in Scenario-1. Heat-map errors are plotted for the compared methods: from left to right, AvatarJLM [46], AGRoL-Diffusion [13], SAGE-Net [15], ours (*Mem-MLP-41*) and the ground-truth.

Method	<b>MPJRE</b> ↓	MPJPE ↓	<b>MPJVE</b> ↓	Jitter ↓
VAE-HMD [11]	-	7.45	-	_
AvatarPoser [19]	4.70	6.38	34.05	10.21
AGRoL-Diffusion [13]	4.30	6.17	24.40	8.32
AvatarJLM [46]	4.30	4.93	26.17	7.19
BoDiffusion [9]	4.53	5.78	21.37	3.50
HMD-Poser [10]	4.27	5.44	30.15	5.62
SAGE Net [15]	4.62	5.86	33.54	7.13
AGRoL-MLP-196 [13]	4.33	6.66	33.58	21.74
Mem-MLP-41 (ours)	4.33	5.24	23.70	7.23
Mem-MLP-60 (ours)	4.02	5.13	22.60	6.06

Table 2. Comparison with state-of-the-art methods for full-body motion estimation. Results on Scenario-2 (S2) are reported on AMASS dataset for MPJVE [cm/s], MPJPE [cm], MPJRE [deg] and Jitter [m/s³]. The best results are in **bold**, and the second best results are underlined.

kicking, jumping, twisting, and dancing are either not represented or underrepresented in the Transition [27] dataset. This lack of motion variety may hinder a thorough assessment of the models' scalability, potentially leading to less reliable evaluation outcomes.

**Evaluation Results on Scenario-3 (S3):** Table 3 presents the evaluation results for Scenario-S3. Our *Mem-MLP* model demonstrates superior performance across all metrics, further validating its superiority. Notably, our model achieves outstanding results in MPJVE, outperforming even

state-of-the-art methods such as AvatarJLM [46] and SAGE Net [15]. This highlights the capability of our model to generate smoother and more natural motion estimates. Note that some of the models listed in Table 4.3 are absent from Table 3 as they were not made available in the original publication.

Accuracy vs Inference Time: We compare MPJRE in Scenario-1 (S1) against on-device inference time measured in frames per second (FPS) in Fig. 1. Specifically, various baseline models are deployed on the Quest-3 device. Notably, our model achieves the maximum FPS value of 72, the minimum required runtime efficiency limit for ensuring smooth and seamless interaction. Avatarposer [19] is also suitable for real-time applications, as it achieves similar FPS performance as our model. However, its predictive accuracy is significantly low, with notably high error rates, making it less reliable for tasks requiring precise motion estimation. Additionally, AGRoL-Diffusion [13] achieves only 3.5 FPS, rendering it unsuitable for real-time deployment due to its limited computational efficiency. In contrast, running at 29 FPS on the device, AGRoL-MLP [13] is a more feasible option for deployment, but it is still well under the minimum required rendering efficiency due to its larger time window input. Notably, our model stands out as

Method	$\mathbf{MPJRE}\downarrow$	<b>MPJPE</b> ↓	<b>MPJVE</b> ↓	Hand PE $\downarrow$	Upper PE↓	<b>Lower PE</b> ↓	Root PE ↓	Jitter↓
Avatarposer [19]	2.72	3.37	21.00	2.12	1.63	5.87	2.90	10.24
AGRoL-Diffusion [13]	2.83	3.80	17.76	1.62	1.66	6.90	3.53	10.08
AvatarJLM [46]	3.14	3.39	15.75	0.69	1.48	6.13	3.04	5.33
SAGE Net [15]	2.41	2.95	16.94	1.15	1.28	5.37	2.74	5.27
AGRoL-MLP-196 [13]	3.09	4.31	109.29	1.79	1.80	7.95	3.86	12.18
Mem-MLP (ours)	2.27	2.54	11.38	0.23	1.08	4.66	2.47	5.10

Table 3. Comparison with state-of-the-art methods for full-body motion estimation. Results on Scenario-3 (S3) are reported on AMASS dataset for Jitter [m/s³], MPJVE [cm/s], MPJPE [cm], Hand PE [cm], Upper PE [cm], Lower PE [cm] and MPJRE [deg]. The best results are in **bold**, and the second best results are <u>underlined</u>.

Method	MPJRE ↓	MPJPE ↓	MPJVE ↓	Jitter↓
XMulti-Head , XMemory-Block	2.76	4.13	35.77	22.70
✗Multi-Head , ✓Memory-Block	2.53	3.72	19.57	8.42
✓Multi-Head , ✓Memory-Block	2.58	3.43	18.17	7.79
✓ Multi-Head , ✓ Memory-Block	2.57	3.08	15.02	6.03

Table 4. Impact of Multi-Head Predictor and Memory Block. Results provide comparisons for the different configurations of our model.

one of the best top-performing models, uniquely combining real-time runtime capabilities on XR headsets with high accuracy levels. We also visualize *Mem-MLP* results on the Quest-3 headset in Fig. 5 for diverse motion cases.

### 4.4. Ablation Study

# Impact of Multi-Head Predictor and Memory Block:

In this section, we present an ablation study to analyze the impact of multi-head predictor and memory block for our Mem-MLP model under the Scenario-1 (S1). For this purpose, we train a MLP model that corresponds to the AGRoL-MLP-41 [13] with a smaller time window (i.e., 41) to reduce the computational overhead compared to its original version. We evaluate the impact of Multi-Head Predictor and Memory-Block on this base model. As shown in Tab. 4, the smaller time window size negatively impacts the performance of the original AGRoL-MLP model [13], which is trained on a longer window size to generate smooth motion sequences. In particular, Jitter increases significantly from 13.01 to 22.70 for the one trained with a smaller window size. To address this issue, we introduce a Memory Block that integrates past information to the hidden layers of backbone, while ensuring that the computational complexity remains acceptable. The second row represents the impact of Memory block using only the rotation branch. The results validate that Memory-block leads to significant improvements in both the MPJVE (from 35.77 to 19.57) and Jitter (from 22.70 to 8.42) metrics. Furthermore, the impact of multi-head predictor is reported in the third row of Tab. 4. The results demonstrate that the performance for all metrics are also improved compared to the base model. Lastly, we combine Memory-Block and Multi-Head Predictor and report their performance in the last row. The results validate that combining both of our contributions achieves the state-of-the-art results.

Automatic Loss Weighting	MPJRE ↓	MPJPE ↓	MPJVE ↓	Jitter ↓
Х	2.60	3.28	17.40	7.46
✓	2.57	3.08	15.02	6.03

Table 5. Impact of Loss Weighting Mechanism. The results show that the automatic loss weighting mechanism is important for the state-of-the-art performance.

Impact of Loss Weighting Mechanism: Our model is trained using multiple losses, where each loss function serves a crucial purpose. However, these losses can be conflicting, which can hinder the training process. To address this issue, we leverage homoscedastic uncertainty to modulate the contributions of each loss. By doing so, we enable the model to adaptively learn the optimal loss weights during training, allowing it to balance the competing objectives and improve overall performance. Specifically, to demonstrate the impact of this weighting mechanism, we perform an additional ablation experiment. In this experiment, we employ manually selected loss weights, optimized through a grid search, for each loss in our objective function. From grid-search, we set  $\lambda_{\theta} = 1$ ,  $\lambda_{rv} = 30$ ,  $\lambda_{p} = 0.5$ ,  $\lambda_{fv} = 0.1$ , and  $\lambda_h = 0.1$ . Table 5 shows the results for this experiment. As demonstrated, the automatic loss weighting mechanism significantly improves the performance of our model across all metrics, particularly, a notable enhancement for the Jitter metric.

#### 5. Conclusions

In this paper, we introduce a novel method, *Mem-MLP*, for generating 3D full-body motions from sparse inputs, achieving state-of-the-art accuracy while being sufficiently lightweight for real-time applications. In particular, our method leverages an MLP backbone with residual connections and introduces a novel component called Memory-Block that represents missing sensor inputs with trainable code-vectors. Ultimately, temporal consistency and smoothness are improved with the code-vectors and sparse signals from previous time instances. Furthermore, we formulate our solution as a multi-task learning problem, where losses from rotation and orientation predictions are jointly optimized. The experiments on the AMASS dataset demonstrate that the superiority of our method over SOTA methods in terms of model complexity and model accuracy.

### References

- [1] Osu accad. https://accad.osu.edu/research/ motion-lab/system-data. 5
- [2] Carnegie mellon university. cmu mocap dataset. 5
- [3] Eyes, japan co. ltd. mocapdata.com. 5
- [4] Metahorizon: Testing and performance analysis, https://developers.meta.com/horizon/documentation/unity/unity-perf/. 2
- [5] Sfu motion capture database. https://mocap.cs. sfu.ca/. 5
- [6] Ijaz Akhter and Michael J Black. Pose-conditioned joint angle limits for 3d human pose reconstruction. In *Proceedings of the IEEE conference on computer vision and pattern recognition*, pages 1446–1455, 2015. 5
- [7] Sadegh Aliakbarian, Pashmina Cameron, Federica Bogo, Andrew Fitzgibbon, and Thomas J. Cashman. Flag: Flowbased 3d avatar generation from sparse observations. In Proceedings of the IEEE/CVF Conference on Computer Vision and Pattern Recognition (CVPR), pages 13253–13262, 2022.
- [8] Sadegh Aliakbarian, Fatemeh Saleh, David Collier, Pashmina Cameron, and Darren Cosker. Hmd-nemo: Online 3d avatar motion generation from sparse observations. In *Proceedings of the IEEE/CVF International Conference on Computer Vision (ICCV)*, pages 9622–9631, 2023. 2
- [9] Angela Castillo, Maria Escobar, Guillaume Jeanneret, Albert Pumarola, Pablo Arbeláez, Ali Thabet, and Artsiom Sanakoyeu. Bodiffusion: Diffusing sparse observations for full-body human motion synthesis. In *Proceedings of the IEEE/CVF International Conference on Computer Vision*, pages 4221–4231, 2023. 6, 7, 13
- [10] Peng Dai, Yang Zhang, Tao Liu, Zhen Fan, Tianyuan Du, Zhuo Su, Xiaozheng Zheng, and Zeming Li. Hmd-poser: On-device real-time human motion tracking from scalable sparse observations. In *Proceedings of the IEEE/CVF Conference on Computer Vision and Pattern Recognition* (CVPR), pages 874–884, 2024. 2, 3, 7, 13
- [11] Andrea Dittadi, Sebastian Dziadzio, Darren Cosker, Ben Lundell, Thomas J. Cashman, and Jamie Shotton. Full-body motion from a single head-mounted device: Generating smpl poses from partial observations. In *Proceedings of the IEEE/CVF International Conference on Computer Vision (ICCV)*, pages 11687–11697, 2021. 2, 3, 5, 7
- [12] Kun Dong, Jian Xue, Zehai Niu, Xing Lan, Ke Lu, Qingyuan Liu, and Xiaoyu Qin. Realistic full-body motion generation from sparse tracking with state space model. In *Proceedings of the 32nd ACM International Conference on Multimedia*, pages 4024–4033, 2024. 2, 3, 6, 7, 13
- [13] Yuming Du, Robin Kips, Albert Pumarola, Sebastian Starke, Ali Thabet, and Artsiom Sanakoyeu. Avatars grow legs: Generating smooth human motion from sparse tracking inputs with diffusion model. In *Proceedings of the IEEE/CVF Conference on Computer Vision and Pattern Recognition*, pages 481–490, 2023. 2, 3, 4, 5, 6, 7, 8, 13, 14, 15, 16, 17, 18, 19
- [14] Yinglin Duan, Tianyang Shi, Zhengxia Zou, Yenan Lin, Zhehui Qian, Bohan Zhang, and Yi Yuan. Single-shot motion completion with transformer, 2021. 3

- [15] Han Feng, Wenchao Ma, Quankai Gao, Xianwei Zheng, Nan Xue, and Huijuan Xu. Stratified avatar generation from sparse observations. In *Proceedings of the IEEE/CVF Conference on Computer Vision and Pattern Recognition*, pages 153–163, 2024. 2, 3, 4, 5, 6, 7, 8, 13, 14, 15, 16, 17, 18, 19
- [16] Saeed Ghorbani, K Mahdaviani, Anne Thaler, K Kording, DJ Cook, G Blohm, and NF Troje. Movi: A large multipurpose motion and video dataset. arxiv 2020. arXiv preprint arXiv:2003.01888, 2020. 5
- [17] Chuan Guo, Xinxin Zuo, Sen Wang, Shihao Zou, Qingyao Sun, Annan Deng, Minglun Gong, and Li Cheng. Action2motion: Conditioned generation of 3d human motions. In *Proceedings of the 28th ACM International Conference on Multimedia*, pages 2021–2029, 2020. 3
- [18] Catalin Ionescu, Dragos Papava, Vlad Olaru, and Cristian Sminchisescu. Human3. 6m: Large scale datasets and predictive methods for 3d human sensing in natural environments. *IEEE transactions on pattern analysis and machine* intelligence, 36(7):1325–1339, 2013. 3
- [19] Jiaxi Jiang, Paul Streli, Huajian Qiu, Andreas Fender, Larissa Laich, Patrick Snape, and Christian Holz. Avatarposer: Articulated full-body pose tracking from sparse motion sensing. In *European conference on computer vision*, pages 443– 460. Springer, 2022. 1, 2, 3, 4, 5, 6, 7, 8, 13, 14
- [20] Jiaxi Jiang, Paul Streli, Xuejing Luo, Christoph Gebhardt, and Christian Holz. Manikin: biomechanically accurate neural inverse kinematics for human motion estimation. In *European Conference on Computer Vision*, pages 128–146. Springer, 2024. 2, 7, 13, 14
- [21] Jiaxi Jiang, Paul Streli, Manuel Meier, and Christian Holz. Egoposer: Robust real-time egocentric pose estimation from sparse and intermittent observations everywhere. In European Conference on Computer Vision, pages 277–294. Springer, 2024. 2, 6, 7, 13
- [22] Alex Kendall, Yarin Gal, and Roberto Cipolla. Multi-task learning using uncertainty to weigh losses for scene geometry and semantics. In *Proceedings of the IEEE conference on* computer vision and pattern recognition, pages 7482–7491, 2018. 5
- [23] Jihyun Lee, Weipeng Xu, Alexander Richard, Shih-En Wei, Shunsuke Saito, Shaojie Bai, Te-Li Wang, Minhyuk Sung, Tae-Kyun Kim, and Jason Saragih. Rewind: Real-time egocentric whole-body motion diffusion with exemplar-based identity conditioning. In *Proceedings of the Computer Vi*sion and Pattern Recognition Conference, pages 7095–7104, 2025. 2
- [24] Sunmin Lee, Sebastian Starke, Yuting Ye, Jungdam Won, and Alexander Winkler. Questenvsim: Environment-aware simulated motion tracking from sparse sensors. In ACM SIG-GRAPH 2023 Conference Proceedings, pages 1–9, 2023. 2
- [25] Matthew Loper, Naureen Mahmood, and Michael J Black. Mosh: motion and shape capture from sparse markers. ACM Trans. Graph., 33(6):220–1, 2014. 5
- [26] Matthew Loper, Naureen Mahmood, Javier Romero, Gerard Pons-Moll, and Michael J Black. Smpl: A skinned multiperson linear model. In Seminal Graphics Papers: Pushing the Boundaries, Volume 2, pages 851–866. 2023. 3

- [27] Naureen Mahmood, Nima Ghorbani, Nikolaus F Troje, Gerard Pons-Moll, and Michael J Black. Amass: Archive of motion capture as surface shapes. In *Proceedings of the IEEE/CVF international conference on computer vision*, pages 5442–5451, 2019. 2, 3, 5, 6, 7
- [28] Christian Mandery, Ömer Terlemez, Martin Do, Nikolaus Vahrenkamp, and Tamim Asfour. The kit whole-body human motion database. In 2015 International Conference on Advanced Robotics (ICAR), pages 329–336. IEEE, 2015. 5
- [29] Meinard Müller, Tido Röder, Michael Clausen, Bernhard Eberhardt, Björn Krüger, and Andreas Weber. Mocap database hdm05. Institut für Informatik II, Universität Bonn, 2(7), 2007. 5
- [30] Ana Filipa Rodrigues Nogueira, Hélder P Oliveira, and Luís F Teixeira. Markerless multi-view 3d human pose estimation: A survey. *Image and Vision Computing*, page 105437, 2025. 1
- [31] Boris N Oreshkin, Antonios Valkanas, Félix G Harvey, Louis-Simon Ménard, Florent Bocquelet, and Mark J Coates. Motion in-betweening via deep \ delta-interpolator. IEEE Transactions on Visualization and Computer Graphics, 2023, 3
- [32] Mathis Petrovich, Michael J Black, and Gül Varol. Temos: Generating diverse human motions from textual descriptions. In *European Conference on Computer Vision*, pages 480–497. Springer, 2022. 3
- [33] Zhiyuan Ren, Zhihong Pan, Xin Zhou, and Le Kang. Diffusion motion: Generate text-guided 3d human motion by diffusion model. In ICASSP 2023 2023 IEEE International Conference on Acoustics, Speech and Signal Processing (ICASSP), pages 1–5, 2023. 3
- [34] Yonatan Shafir, Guy Tevet, Roy Kapon, and Amit H Bermano. Human motion diffusion as a generative prior. arXiv preprint arXiv:2303.01418, 2023. 3
- [35] Leonid Sigal, Alexandru O Balan, and Michael J Black. Humaneva: Synchronized video and motion capture dataset and baseline algorithm for evaluation of articulated human motion. *International journal of computer vision*, 87(1):4–27, 2010. 6
- [36] Sebastian Starke, Ian Mason, and Taku Komura. Deepphase: Periodic autoencoders for learning motion phase manifolds. *ACM Transactions on Graphics (TOG)*, 41(4):1–13, 2022. 3
- [37] Jiangnan Tang, Jingya Wang, Kaiyang Ji, Lan Xu, Jingyi Yu, and Ye Shi. A unified diffusion framework for scene-aware human motion estimation from sparse signals. In *Proceedings of the IEEE/CVF Conference on Computer Vision and Pattern Recognition*, pages 21251–21262, 2024. 2
- [38] Nikolaus F Troje. Decomposing biological motion: A framework for analysis and synthesis of human gait patterns. *Jour*nal of vision, 2(5):2–2, 2002. 5
- [39] Matthew Trumble, Andrew Gilbert, Charles Malleson, Adrian Hilton, and John P Collomosse. Total capture: 3d human pose estimation fusing video and inertial sensors. In *BMVC*, pages 1–13. London, UK, 2017. 5
- [40] Aaron van den Oord, Oriol Vinyals, and koray kavukcuoglu. Neural discrete representation learning. In Advances in Neural Information Processing Systems. Curran Associates, Inc., 2017. 2, 12

- [41] Timo Von Marcard, Bodo Rosenhahn, Michael J Black, and Gerard Pons-Moll. Sparse inertial poser: Automatic 3d human pose estimation from sparse imus. In *Computer graphics forum*, pages 349–360. Wiley Online Library, 2017. 1, 2
- [42] Alexander Winkler, Jungdam Won, and Yuting Ye. Questsim: Human motion tracking from sparse sensors with simulated avatars. In *SIGGRAPH Asia 2022 Conference Papers*, pages 1–8, 2022. 2
- [43] Songpengcheng Xia, Yu Zhang, Zhuo Su, Xiaozheng Zheng, Zheng Lv, Guidong Wang, Yongjie Zhang, Qi Wu, Lei Chu, and Ling Pei. Envposer: Environment-aware realistic human motion estimation from sparse observations with uncertainty modeling. In *Proceedings of the Computer Vision and Pat*tern Recognition Conference, pages 1839–1849, 2025. 2
- [44] Dongseok Yang, Doyeon Kim, and Sung-Hee Lee. Real-time lower-body pose prediction from sparse upper-body tracking signals. *arXiv preprint arXiv:2103.01500*, 2021. 1, 2
- [45] Mingyuan Zhang, Zhongang Cai, Liang Pan, Fangzhou Hong, Xinying Guo, Lei Yang, and Ziwei Liu. Motiondiffuse: Text-driven human motion generation with diffusion model. *arXiv preprint arXiv:2208.15001*, 2022. 3
- [46] Xiaozheng Zheng, Zhuo Su, Chao Wen, Zhou Xue, and Xiaojie Jin. Realistic full-body tracking from sparse observations via joint-level modeling. In *Proceedings of the IEEE/CVF International Conference on Computer Vision*, pages 14678–14688, 2023. 2, 3, 5, 7, 8, 13, 15, 16, 17, 18, 19
- [47] Yi Zhou, Connelly Barnes, Jingwan Lu, Jimei Yang, and Hao Li. On the continuity of rotation representations in neural networks. In *Proceedings of the IEEE/CVF conference on* computer vision and pattern recognition, pages 5745–5753, 2019. 4

# Mem-MLP: Real-Time 3D Human Motion Generation from Sparse Inputs

# Supplementary Material

Method	MPJPE ↓	Upper PE ↓	Lower PE ↓	Jitter ↓
Rotation Branch	3.36	1.56	5.97	7.34
Position Branch	3.07	1.24	5.72	5.45
Rotation + Position Branch	3.08	1.25	5.72	6.03

Table 6. Experiments on inverse kinematics. We run an optimized inverse kinematics solution to correct the estimated angles (rotation branch) using 3D joint locations (position branch) as target points.

#Layers (PB)	#Layers (RB)	$\mathbf{MPJRE}\downarrow$	MPJPE ↓	$\mathbf{MPJVE}\downarrow$	Jitter ↓
1	1	2.60	3.14	15.15	6.04
2	2	2.57	3.08	15.02	6.03
4	4	2.57	3.11	15.04	6.41

Table 7. Experiments on layer depth of multi-task predictor. PB and RB denote position and rotation branches.

Method	<b>MPJRE</b> ↓	<b>MPJPE</b> ↓	<b>MPJVE</b> ↓	Jitter ↓
MHP w/ MB	2.59	3.40	17.80	5.57
MHP wo/ MB	2.57	3.08	15.08	6.03

Table 8. Effect of Memory-Block (MB) integration into Multi-Head Predictor (MHP).

In the ablation study, we also conduct additional experiments on memory block, multi-task predictor, number of MLP blocks, sequence length, impact of VQ-VAE and comparison with LSTM and GRU alternatives. All methods are evaluated for Scenario-1 (S1).

# A. Architectural Design

**Inverse Kinematics:** We observe that the estimated 3D joint positions generated by the second branch of our multihead predictor are more accurate than those from the first branch. However, since the SMPL model cannot directly reconstruct 3D body pose representations from joint positions alone, we employ an inverse kinematics (IK) solver using the L-BFGS optimization method, achieving optimal results within 15 iterations. The IK solver optimizes joint rotations by initializing with the output of the rotation branch and targeting the more accurate 3D joint positions from the second branch. The corresponding results are presented in Table 6.

**Layer Depth of Multi-Task Predictor:** In Table 7 we evaluate the effect of different numbers of MLP blocks per branch. Our default configuration (2 layers) yields the best trade-off, especially reducing Jitter by 16.1% over 1-layer and 13.9% over 4-layer configurations.

**Layer Depth of MLP Backbone:** We conduct experiments

$\mathbf{MLP} \ \mathbf{Blocks} \ L$	$\mathbf{MPJRE} \downarrow$	$\mathbf{MPJPE} \downarrow$	$\mathbf{MPJVE} \downarrow$	Jitter $\downarrow$	FLOPS $\downarrow$
8	2.57	3.08	15.02	6.03	0.25G
10	2.58	3.07	14.78	6.19	0.27G
12	2.59	3.11	14.88	6.10	0.30 <b>G</b>

Table 9. Effect of Number of MLP blocks  ${\cal L}$  on model predictive accuracy.

Seq. Length $T$	<b>MPJRE</b> ↓	MPJPE ↓	MPJVE ↓	Jitter↓
11	2.60	3.27	20.81	15.05
21	2.61	3.19	16.82	8.22
41	2.57	3.08	15.02	6.03
60	2.56	3.05	14.27	5.35

Table 10. Impact of sequence length T on model performance.

Method	MPJRE ↓	MPJPE ↓	MPJVE ↓	Jitter↓
Mem-MLP w/o VQ-VAE	2.60	3.16	15.35	6.61
Mem-MLP w/ VQ-VAE	2.57	3.08	15.08	6.03

Table 11. Effect of VQ-VAE in Memory Block.

with different number of MLP blocks in the backbone of our architecture. As presented in 9, our default configuration (L=8) presents better MPJRE and Jitter results, while (L=10), shows an improvement in MPJPE and MPJVE metrics, but increases the computational overhead in our model, which falls slightly under real-time performance.

**Integration of Memory-Block to Multi-Head Predictor:** It is observed that, Table 8, including MB in MHP improves temporal consistency (lower Jitter), although MPJRE and MPJPE are slightly worse. This shows that MB smooths the motion by leveraging past context.

**Impact of Sequence Length:** Longer sequences improve performance (especially Jitter and MPJVE), but increase computation, Table 10. This trade-off must be tuned depending on application constraints.

Impact of VQ-VAE: To better understand the impact of code-vector  $\mathcal{E}_l$  in the Memory Block of our architecture we conduct another experiment where we remove the codevector from our Memory Block, and the feature  $\mathbf{Z}_m$  is given by the following equation:  $\mathbf{Z}_m = \mathbf{m} * \mathbf{Z}_{\theta}$ . Table 11 shows that the incorporation of code-vector  $\mathcal{E}_l$  in our Memory Block enhances the predictive accuracy of our model in all metrics. In our experiments, we set the dimension of the code-vector to 64.

**VQ-VAE Details:** Below we report extra details on the VQ-VAE model. The overall architecture is illustrated in

Model	$\mathcal{L}_{\mathrm{enc}}$	MPJPE ↓	Upper PE↓	Lower PE ↓	Jitter ↓
Mem-MLP	2	2.59	3.11	15.13	6.08
Mem-MLP	4	2.57	3.08	15.02	6.03
Mem-MLP	6	2.58	3.15	15.34	6.21

Table 12. Experiments on different sizes of  $\mathbf{L_{enc}}$  and their impact on Mem-MLP.

Figure 1. We adopt a lightweight MLP-based design: each MLP block comprises layer normalization, a single linear layer and a SiLU activation; this block is used uniformly in both the encoder and decoder. The encoder depth is denoted  $L_{enc}$ , with baseline value  $L_{enc} = 4$ , the decoder depth  $L_{dec}$ , with baseline value  $L_{dec} = 1$  and the latent dimensionality is  $d_{z_s} = 256$  of the model. The training is performed trying to minimize a loss that consists of two terms, the rotation reconstruction loss (Equation 1), and the commitment loss introduced in [40], which encourages the encoder outputs to commit to specific codebook entries. The discrete codebook is denoted  $\mathcal{C} = \{\mathbf{e}_1, \dots, \mathbf{e}_K\} \subset \mathbb{R}^{d_{z_s}}$ , where K=64 is the number of codebook entries in our best performing Mem-MLP models. This choice yields a compact yet expressive discrete representation suitable for downstream reconstruction and prior modeling. Mem-MLP pipeline is only using the pre-trained, frozen, encoder of a VQ-VAE model during training and inference. This design reduces training time while improving accuracy. We also experimented with joint training of the VQ-VAE and Mem-MLP, but observed substantial performance degradation. We train the VQ-VAE for 100 epochs using the Adam optimizer with batch size 256. The Adam hyperparameters are set to  $\beta = (0.9, 0.99)$  and a weight decay of  $10^{-4}$ . The initial learning rate is  $1 \times 10 - 4$  and it is decreased by a factor of 0.2 at scheduled milestone epochs [20, 50, 70].

**VQ-VAE Configuration Settings:** To quantify the sensitivity of downstream performance to the VQ-VAE configuration, we perform ablation experiments over codebook sizes  $K \in 32,64,128$  and the encoder depths  $\mathbf{L_{enc}} \in 2,4,6$ . For each VQ-VAE variant we freeze the learned codebook and integrate the corresponding discrete priors into the final Mem-MLP model. More specifically, Table 12 presents the results for varying encoder depths  $\mathbf{L_{enc}}$ , while keeping all other VQ-VAE hyper-parameters ( $\mathbf{L_{dec}}, d_{z_s}$ , and K = 64) fixed. Each trained VQ-VAE is subsequently employed within Mem-MLP, where a new model is trained from scratch under the corresponding configuration. In parallel, Table 13 reports the ablation results on the VQ-VAE codebook size K, with all remaining hyperparameters held constant.

**Comparison with LSTM & GRU Memory Blocks:** To further assess the effectiveness of our approach, we implemented recurrent memory variants by replacing the memory block with LSTM- or GRU-based layers. The archi-

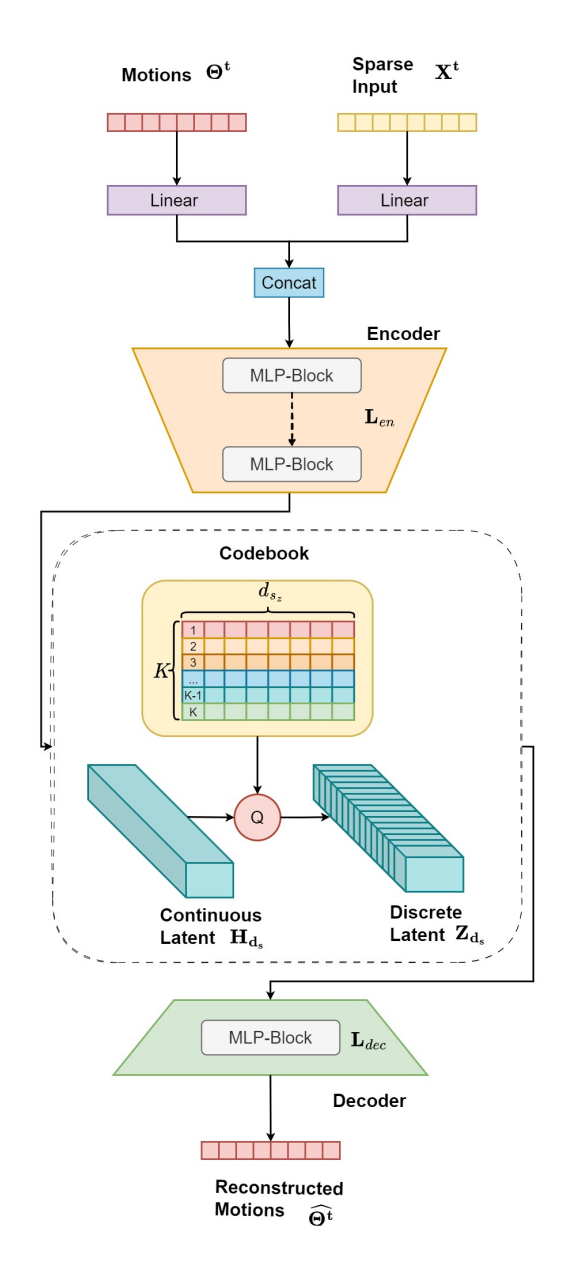


Figure 7. VQ-VAE architecture diagram

Model	K	MPJPE ↓	Upper PE↓	Lower PE ↓	Jitter
Mem-MLP	32	2.57	3.13	15.30	6.14
Mem-MLP	64	2.57	3.08	15.02	6.03
Mem-MLP	128	2.62	3.20	15.55	6.52

Table 13. Experiments on different sizes of K, and their impact on Mem-MLP.

tecture is extended with a recurrent memory block that applies Layer Normalization to the input sparse features, followed by either an LSTM or GRU layer, and a SiLU activation function. During training, the recurrent units are initialized differently depending on the configuration: (a) LSTM-

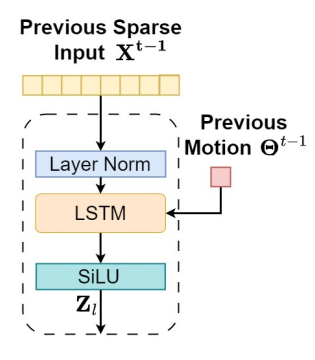


Figure 8. LSTM-based memory block diagramm.

based memory block: The hidden state is initialized using the final time step of the sparse motion features, thereby incorporating prior motion context, while the cell state is zero-initialized. (b) GRU-based memory block: The hidden state alone is initialized from the final time step of the sparse motion features. Figure 8 provides visual explanation on the LSTM-based memory block structure. In evaluation mode, both LSTM and GRU blocks are run without explicit initialization, relying instead on internally propagated states. Table 15 reports the results, where our method consistently outperforms both RNN-based memory configurations. While the Memory-Block superficially resembles recurrent architectures because it reuses temporal context, its design differs in two critical aspects: (i) it avoids the sequential gating of LSTMs/GRUs, enabling higher parallelism and (ii) it fuses two complementary sources of information, current sparse inputs and VQ-VAE code-vectors (autoregressively providing full-pose priors), yielding richer context than standard recurrence.

**Placement of Memory Blocks in Backbone:** To further assess the impact of memory blocks on the performance of our model, we conduct an ablation study focusing on their placement within the backbone. Specifically, in our model, memory blocks are incorporated in some of the layers of backbone for computational efficiency. In particular, we introduce Memory-blocks in 2<sup>nd</sup>, 4<sup>th</sup>, 6<sup>th</sup>, and/or 8<sup>th</sup> layers of the backbone. The results presented in Table 14 illustrate the effect of progressively adding memory blocks to the backbone via different layers. From the results, we observe a constant improvement in performance as more memory block outputs are introduced into deeper layers of the backbone. Notably, incorporating memory blocks at all four layers obtains the best scores for MPJRE, MPJPE, and MPJVE metrics. However, a slightly lower Jitter score is obtained when memory block is introduced for the 8th layer.

# **B.** Model Size and Complexity

Model Size and Model Complexity: It is crucial to consider the model size and model complexity (i.e., number

Memory Block Layer(s) in Backbone	MPJRE ↓	MPJPE↓	MPJVE ↓	Jitter ↓
2	2.63	3.17	15.12	6.82
2, 4	2.63	3.20	15.57	6.66
2, 4, 6	2.60	3.14	15.04	6.37
2, 4, 6, 8	2.57	3.08	15.02	6.03

Table 14. Impact of placement of memory blocks in backbone. The performance for all metrics improves when memory blocks are incorporated in the deeper layers of our backbone. The best results are in **bold**.

Method	MPJRE ↓	MPJPE ↓	$\mathbf{MPJVE}\downarrow$	Jitter ↓	$FLOPs(G)\downarrow$
GRU-MB	2.63	3.50	19.11	8.77	0.24
LSTM-MB	2.59	3.29	17.40	7.72	0.25
Ours	2.57	3.08	15.02	6.03	0.25

Table 15. Assessment of LSTM and GRU as Alternatives to the Existing Memory Block.

Method	FLOPs ↓	Size (MB) ↓	<b>#Params</b> (M) ↓
AvatarPoser [19]	0.33G	15.73	4.12
AGRoL-MLP [13]	0.88 <b>G</b>	14.25	3.74
AGRoL-Diffusion [13]	1.00 <b>G</b>	28.54	7.48
AvatarJLM [46]	4.64G	243.41	63.81
BoDiffusion [9]	0.46 <b>G</b>	83.70	21.94
SAGE-Net [15]	4.10 <b>G</b>	458.79	120.27
EgoPoser [21]	0.33 <b>G</b>	15.77	4.12
MMD [12]	7.98 <b>G</b>	853.47	101.72
MANIKIN-S [20]	0.33 <b>G</b>	_	4.12
MANIKIN-L [20]	4.64G	_	63.8
MANIKIN-LN [20]	4.64G	_	63.8
HDM-Poser [10]	0.38 <b>G</b>	66.55	9.55
Mem-MLP-41 (Ours)	<b>0.25</b> G	15.38	4.10
Mem-MLP-60 (Ours)	0.38G	16.08	4.59

Table 16. Model size and complexity (FLOPs, parameters, and memory).

of FLOPs) to better assess the computational efficiency and memory footprint. The results in Table 16 highlight the trade-offs between these factors across state-of-the-art methods. Notably, *Mem-MLP* demonstrates a strong balance across all three metrics. With a model size of 15.38 MB, it is the second most compact among the others, slightly higher than AGRoL-MLP [13]. This compactness positively affects the architecture, which minimizes storage requirements. Additionally, *Mem-MLP* achieves the lowest FLOP (0.25G), outperforming all other methods, including AvatarPoser [19], AGRoL-MLP [13], and MANIKIN-S [20], while being significantly more efficient than diffusion-based models such as AGRoL-Diffusion [13], BoDiffusion [9], and MMD [12].

Regarding the number of parameters, *Mem-MLP* (4.10M) is the second lowest after AGRoL-MLP [13] (3.74M) and is notably lighter than diffusion-based models, such as MMD [12] (101.72M) BoDiffusion [9] (21.94M)

Method	CPU (ms) ↓	CPU (FPS) ↑
AvatarPoser [19]	6.0	72.0
AGRoL-MLP [13]	30.1	26.0
AGRoL-Diffusion [13]	290.5	3.5
Mem-MLP-41 (Ours)	<u>6.8</u>	72.0
Mem-MLP-60 (Ours)	8.5	65.0

Table 17. On-device inference time (CPU). Lower is better for time (ms), higher is better for FPS.

and SAGE-Net [15] (120.27M). Additionally, MANIKIN [20] achieves competing predictive accuracy with computational cost. Overall, these results indicate that our *Mem-MLP* model achieves the optimal trade-off between efficiency and model complexity, making it well-suited for resource-constrained environments. Its reduced FLOPs and its compact size suggest that it can operate efficiently in real-time applications with minimal computational overhead.

On-Device Inference Speed: We deployed a subset of methods (i.e., AvatarPoser [19], AGRoL-MLP [13], AGRoL-diffusion [13], and ours) on the Meta Quest 3 to evaluate their on-device performance, Table 17. This allows us to illustrate how each method can operate in real-world, resource-constrained environments. As previously noted, Mem-MLP-41 and AvatarPoser [19] achieve real-time performance, running at 6.8ms and 6.0ms on-device, respectively. Moreover, for Mem-MLP-60, we observe that its execution time slightly increases to 8.5ms, maintaining near real-time performance. Nevertheless, this model remains a viable option for the applications where slightly higher latency is acceptable, when the methods are integrated with frame-interpolation techniques or a better HMD hardware with improved processing capabilities. In the deployment stage, all methods are converted to ONNX models and executed on a single CPU.

# C. Qualitative Results

We visualize the generation results of different methods for various motion types. The results are illustrated in Figs. 9, 10, 11, 12, 13. In particular, we report heat-map errors that ease the visualization errors for the different parts of human-body.

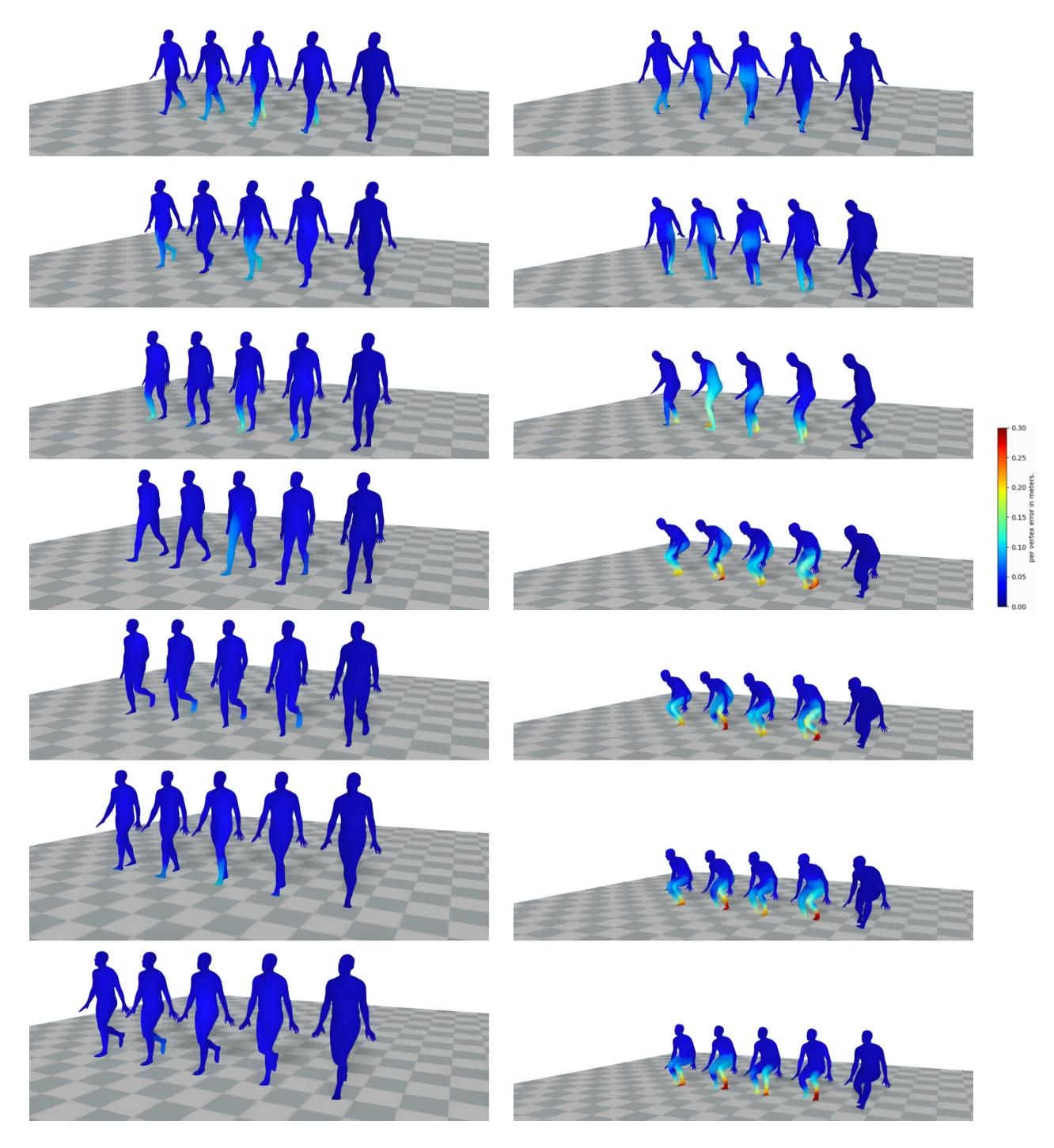


Figure 9. Results on normal walk and sitting motions. Heat-map errors are plotted for different methods. From left to right: Avatar-JLM [46], AGRoL-Diffusion [13], SAGE-Net [15], ours (*Mem-MLP-41*) and the ground-truth.

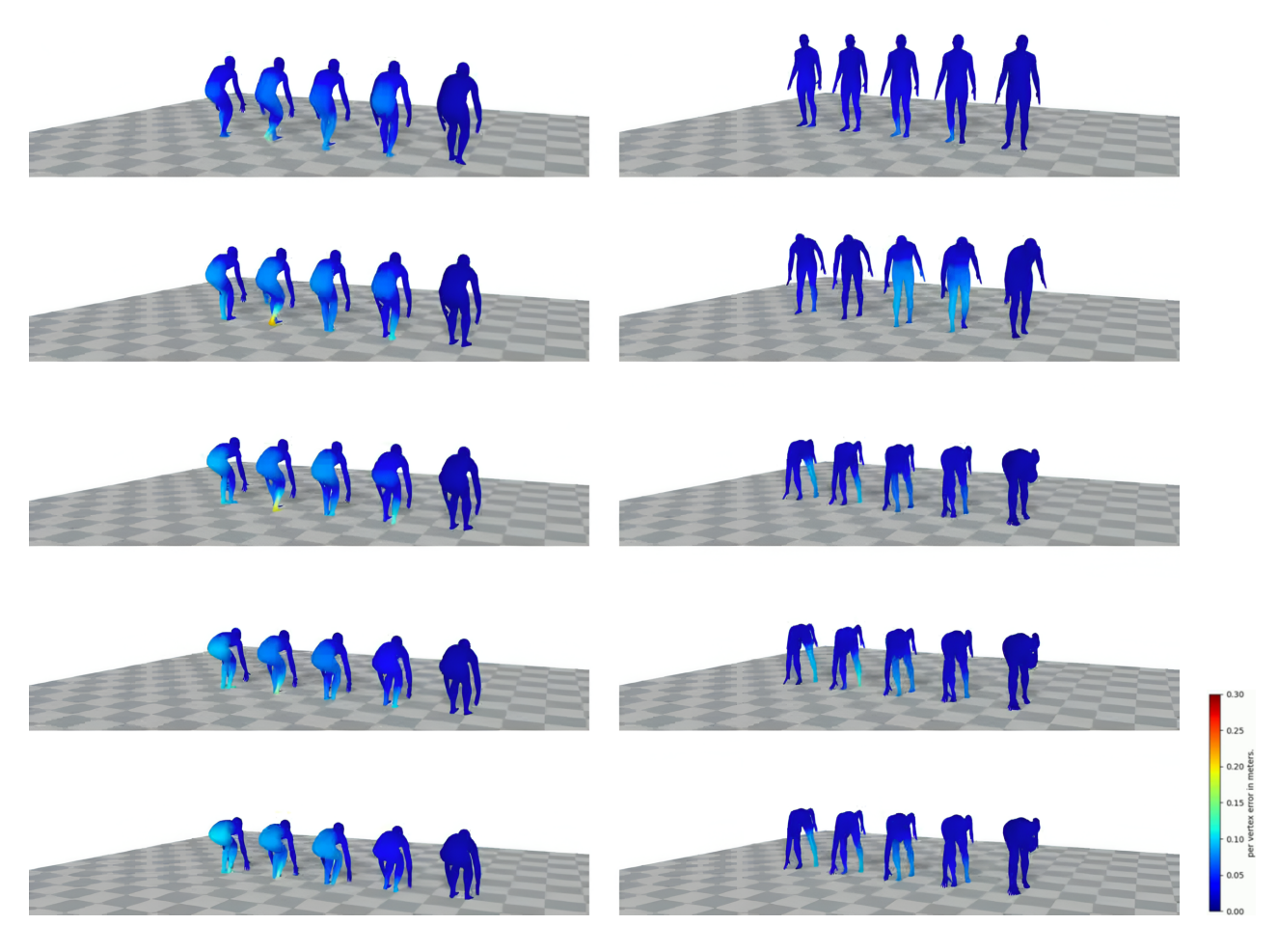


Figure 10. Results on lifting and touching ground motions. Heat-map errors are plotted for different methods. From left to right: AvatarJLM [46], AGRoL-Diffusion [13], SAGE-Net [15], ours (*Mem-MLP-41*) and the ground-truth.

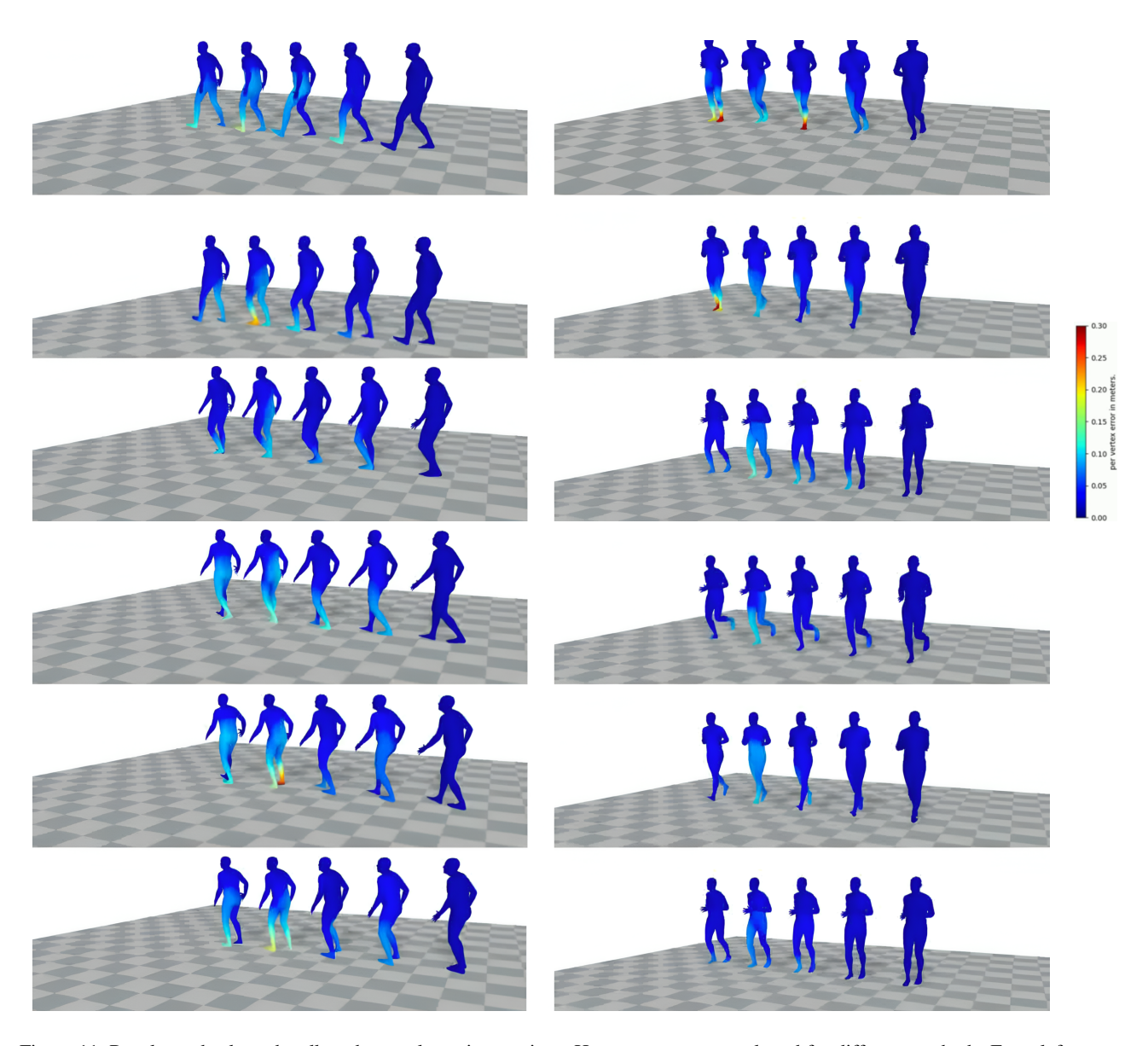


Figure 11. Results on backward walk and normal running motions. Heat-map errors are plotted for different methods. From left to right: AvatarJLM [46], AGRoL-Diffusion [13], SAGE-Net [15], ours (*Mem-MLP-41*) and the ground-truth.

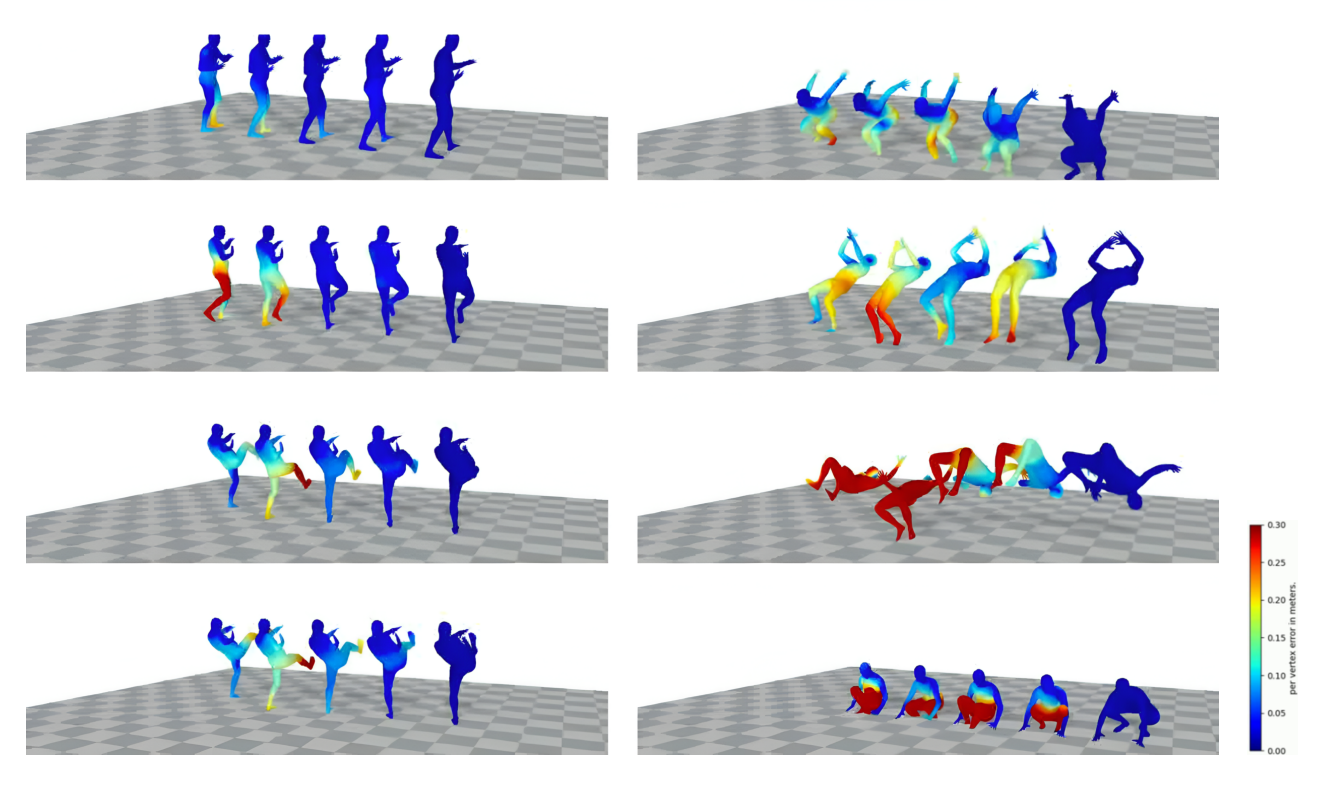


Figure 12. Results on kicking and back-flip ground motions. Heat-map errors are plotted for different methods. From left to right: AvatarJLM [46], AGRoL-Diffusion [13], SAGE-Net [15], ours (*Mem-MLP-41*) and the ground-truth.

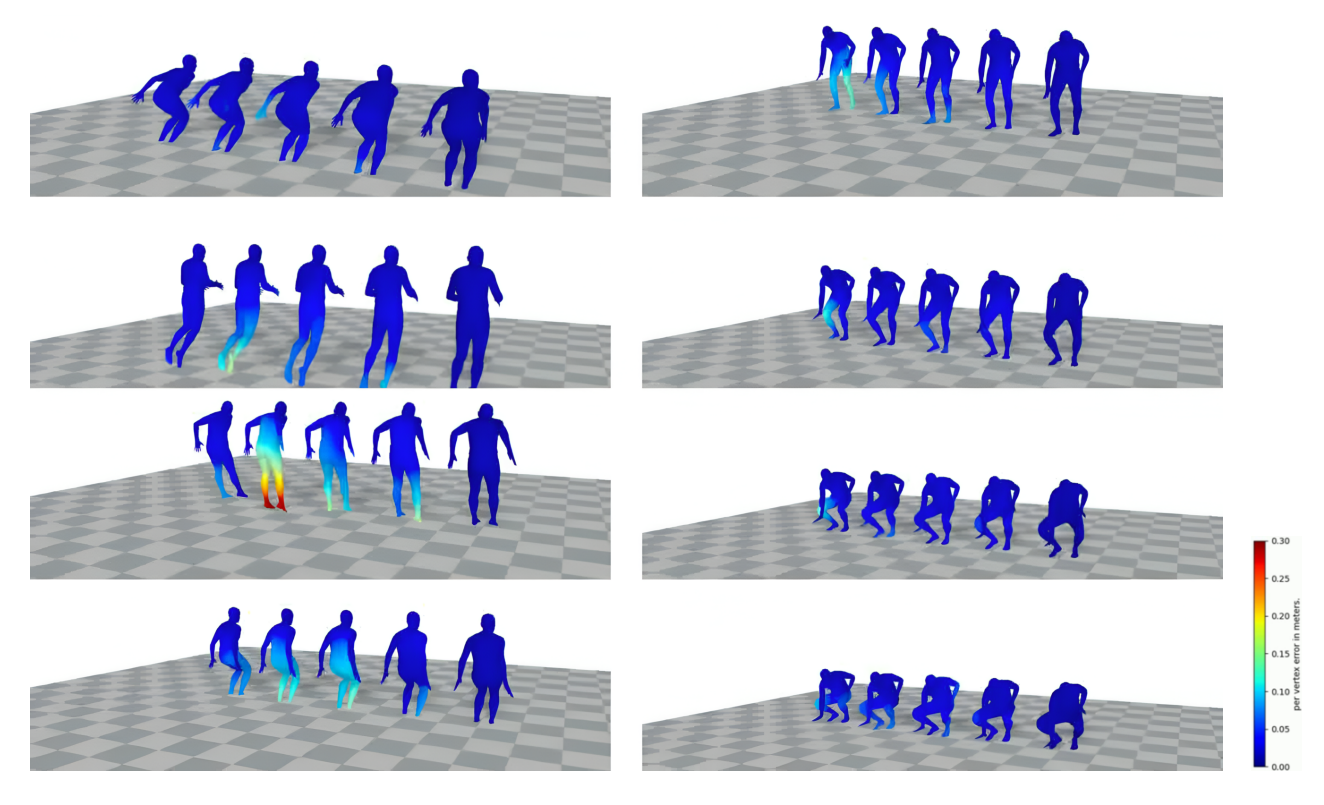


Figure 13. Results on jumping and squating motions. Heat-map errors are plotted for different methods. From left to right: Avatar-JLM [46], AGRoL-Diffusion [13], SAGE-Net [15], ours (*Mem-MLP-41*) and the ground-truth.